Heavy-ion injection in synchrotrons and storage rings

D. Dinev
Institute for Nuclear Research and Nuclear Energy, Bulgarian Academy of Sciences

Fiz. Élem. Chastits At. Yadra **28**, 449–494 (March–April 1997)

A survey of methods for injection of heavy ions in synchrotrons and storage rings is given. The three main injection methods—stacking in the transverse phase space, stacking in the longitudinal phase space, and ion stripping—are described in detail. Combinations of multiturn injection with linear coupling, beam cooling, and rf stacking are represented. Many examples and original results of the author on the simulation of the injection in the Nuclotron booster are given. © *1997 American Institute of Physics.* [S1063-7796(97)00402-6]

1. INTRODUCTION

The last decades have shown a growing interest in investigations with heavy ions. The traditional applications of heavy-ion beams in nuclear-structure studies and new-element synthesis have been considerably broadened and now cover research fields from atomic and molecular physics to beam crystallization. At the same time, nuclear-physics studies have evolved to higher energy, including experiments with ultrarelativistic ion beams.

It is the remarkable progress in accelerator physics and techniques that underlies this development.

The milestones of this progress are the breakthrough in ion-source technology with the creation of the ECR and EBIS sources, the revolutionized impact of the beam cooling technique (electron, stochastic, and laser), and the realization that large proton facilities can be used for ion acceleration after modest upgrade.

Whereas 20 years ago tandems, conventional AVF cyclotrons, and heavy-ion linacs were used for ion acceleration, nowadays the field of heavy-ion facilities cover the following: large AVF cyclotrons, including superconducting machines; a large number of accelerator–cooler–storage rings for low and medium energy; superconducting heavy-ion linacs; existing proton synchrotrons, converted to ion accelerators with energies above 1 GeV/A; and new ion synchrotrons and relativistic-ion colliders.

This paper represents a survey devoted to one of the major steps in the heavy-ion acceleration process—ion injection.

We will restrict ourselves to discussion of injection in heavy-ion synchrotrons and storage rings.

The goal of any injection is to accumulate high-current beams with minimal particle losses, i.e., with high efficiency. The accelerator acceptance should be filled as densely as possible.

Many methods developed for injection of protons are applied also for heavy-ion accumulation.

Thus, fast (single-turn) injection by means of a kicker magnet which is switched on during one revolution is used for injection of heavy ions from booster synchrotrons or in cases when the beam pulse from the ion source is too short (EBIS and laser sources). We will not specially discuss this method here, as it is elucidated, for example, in Ref. 1.

The intensity of the heavy-ion beams produced by the ion sources, especially in high charge states, are limited and as a rule are lower than the intensity of the proton beams.

That is why the methods for multiturn injection are of special importance for heavy-ion storage.

There exist methods for particle stacking in either betatron phase space or synchrotron phase space, or simultaneously in both.

Betatron stacking is discussed in Sec. 2, where we also consider methods of applying beam coupling and beam cooling.

Section 3 is devoted to rf stacking.

Another method for ion accumulation is charge-exchange injection, which is widely used in proton synchrotrons. When applied for injection of heavy ions, this method has many special features, which are discussed in detail in Sec. 4.

Tables I and II summarize data on the injection in some of the heavy-ion synchrotrons and storage rings now in operation.

2. MULTITURN INJECTION WITH BETATRON STACKING

The classical method of multiturn injection with accumulation of particles in the transverse (radial) phase plane is widely used in heavy-ion synchrotrons and storage rings. Some examples are the synchrotron SIS in Darmstadt[2] and the cooler ring CELSIUS in Stockholm.[3]

2.1. Principle of betatron stacking

In the betatron stacking method[4–9] the closed orbit is locally distorted by means of two, three, or four bump magnets in such a way as to pass close to the injection septum (Fig. 1a). At first the bump is as big as possible, and then it is gradually reduced to zero.

In each time interval $t \in (0, nT_s)$, where T_s is the revolution period and n is the number of turns during which injection occurs, a portion (slice) of the incoming beam is injected into the accelerator. In general the slice center will have linear (x_i) and angular (x_i') displacements with respect to the closed orbit, and the slice will undergo betatron oscillations.

One turn later, the slice will return to the injection azimuth. However, owing to the betatron oscillations around the instantaneous closed orbit, most of the particles will avoid the septum. This is clearly seen in the normalized phase

TABLE I. Injection in heavy-ion synchrotrons.

Accelerator	SATURNE 2 LNS, Saclay		SIS GSI, Darmstadt	Synchrophasotron JINR, Dubna	Nuclotron JINR, Dubna	AGS BNL, Brookhaven
Maximum $B\rho$ [Tm]	12.9		18	28	48.5	95
Injector	RFQ+booster MIMAS	a)	UNILAC	linac LU20	linac LU20	1 MeV/A tandem+ booster
		b)	storage ring ESR			
Injection energy [MeV/A]	12.5	a)	11.4	5	5	192
		b)	830			
Type of injection	rf stacking in MIMAS	a)	multiturn+cooling	single turn	single turn	multiturn+coupling in the booster,
	single turn in SATURNE	b)	fast, bunch to bucket			single turn in AGS

plane (x,x^*), with $x^*=\beta x'+\alpha x$, where β and α are the Twiss structural functions. In the normalized phase space (x,x^*) the particle trajectories are circles (Fig. 1b).

For our explanation of the multiturn injection process, let us take the horizontal betatron frequency $Q_x=I+0.25$, where I is any integer. With this value of Q_x the particles of the considered slice will return after four revolutions to their initial positions, i.e., within the septum. Falling again within the septum, the slice would undergo the wrong bend and would be lost in the vacuum chamber. Fortunately, the closed orbit has been meanwhile displaced towards the machine center. If the closed orbit moves slowly enough compared to the period of the betatron oscillations, the particle motion will be adiabatic and the particles will follow the orbit. No additional oscillations will be excited. This is depicted in Fig. 1c, in which three successive positions of the beam slice and closed orbit are shown. If the displacement of the closed orbit during four revolution periods is sufficiently large, the particles of the slice will avoid the septum horizontally and will be accumulated in the accelerator.

Meanwhile, a new portion (slice) of the incoming beam will be injected. The particles of this second slice will have larger amplitudes of the betatron oscillations as the orbit bump is reduced and the injection position is kept unchanged.

The process continues until the bump height is reduced to zero.

It can be shown that the successive slices (or, more precisely, what remains of each slice after its multiple cutting by the septum edge) lie on a spiral (Fig. 1c). The origin of the spiral is on the simultaneous orbit, and at the end of the injection process it coincides with the machine center. In the case of a linear orbit fall, the spiral is a spiral of Archimedes.

Computer simulations can describe the stacking process step by step.[10,11]

As an example, we will discuss in this paper the project of the booster synchrotron for the superconducting heavy-ion synchrotron Nuclotron now under consideration at JINR, Dubna.[12] This will be a six-period synchrotron (Fig. 2) with circumference 50.52 m, capable of accelerating protons up to 650 MeV and ions with $Z/A=0.5$ up to 200 MeV/A. The currently operating linac LU-20 which accelerates protons up to 20 MeV and ions with $Z/A=0.5$ up to 5 MeV/A will be used as an injector into the booster. The booster will increase the beam intensities in the Nuclotron by more than a factor of ten, will raise the final energy of the ions by applying ion stripping, and will improve the beam quality by electron cooling. Other important booster parameters are: beam rigidity at injection 0.647 Tm and maximum 4.3 Tm; betatron tune $Q_h=Q_v=2.25$; emittance of the injected beam 40π mm·mrad; acceptance 260π mm·mrad.

Figures 3 and 4 show the results of computer simulations. Both the radial (x,x') and vertical (y,y') transverse phase planes and the transverse cross section (x,y) are shown. In Fig. 3 the injection covers three revolution periods (the three beam slices are clearly cut in the radial phase plane), while in Fig. 4 it covers 15 periods (the successive slices have a wide overlap, and the density distribution is rather smooth).

TABLE II. Injection in heavy-ion cooler storage rings.

Ring	MIMAS SATURNE Saclay	CRYRING MSI Stockholm	TSR MPI Heidelberg	COOLER IUCF Indiana	TARN 2 INS Tokyo	CELSIUS TSL Uppsala		ESR GSI Darmstadt	COSY KFA Jülich
Maximum $B\rho$ [Tm]	1.0	1.4	1.5	3.6	6.1	7.0		10	12
Injector	EBIS+RFQ	CRYEBIS+ RFQ	tandem+ linac	cyclotron K=220	cyclotron K=70	cyclotron K=180	a) b)	UNILAC SIS	cyclotron K=45
Injection energy [MeV/A]	0.187	0.3	0.5–15	55–220	10–68	45–190	a) b)	1.4 200–320	11–45
Mass range	1–83	2–208	2–130	1–20	1–14	1–16		20–238	1–20
Type of injection	rf stacking	multiturn+ electron cooling	rf stacking+ multiturn	stripping	rf stacking+ multiturn	stripping	a) b)	rf stacking fast, bunch to bucket	stripping

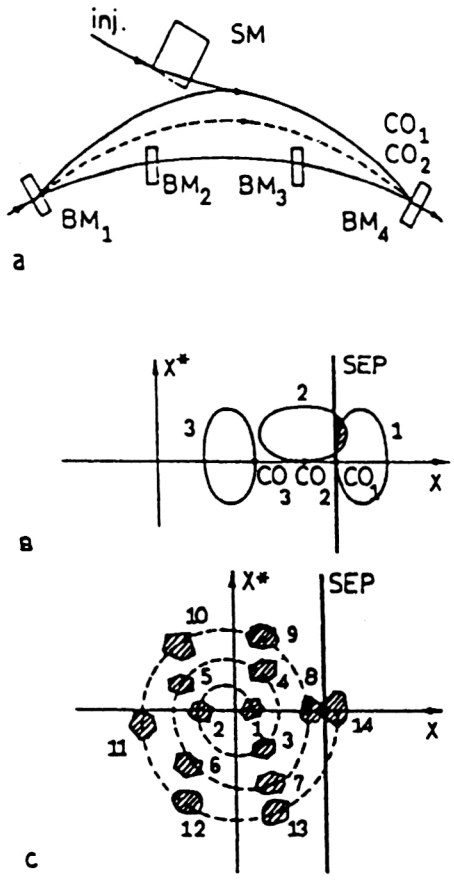

FIG. 1. Principle of betatron stacking: (a) closed orbit bump; (b) the positions of an injected slice at times $t, t+T_s, t+2T_s$. The hatched area will be lost; the fractional part of Q is taken as 0.25. (c) Successive positions of the injected beam slices.

2.2. The local orbit bump

During the multiturn injection, a local orbit bump should be produced in order for the beam to pass close to the septum. Let us consider the kicks in the bump magnets necessary for the local closed-orbit bump to be produced. Here we will analyze the general case of arbitrary phase distances between the elements as given in Ref. 13.

A. Systems with three bumpers

A scheme of three bumpers is depicted in Fig. 5. The kicks ε_1, ε_2, and ε_9 which produce a closed-orbit bump with deviation X_s at the injection azimuth are the solutions of the following system of three equations:

$$\sin \mu_{19}\sqrt{\beta_1}\varepsilon_1+\sin \mu_{29}\sqrt{\beta_2}\varepsilon_2=0,$$

$$\cos \mu_{19}\sqrt{\beta_1}\varepsilon_1+\cos \mu_{29}\sqrt{\beta_2}\varepsilon_2+\sqrt{\beta_9}\varepsilon_9=0,$$

$$\sin \mu_{99}\sqrt{\beta_9}\varepsilon_9=\frac{X_9}{\sqrt{\beta_9}}, \tag{2.2.1}$$

where $\varepsilon_1=B_1 l_1/B\rho$ is the kick in the first bumper, and μ_{12} is the phase advance between BM_1 and BM_2 ($\mu_{12}=\int_1^2 ds/\beta(s)$).

B. System with four bumpers

Using a system with four bumpers, the additional constraint of having a zero slope at the injection azimuth can be imposed (Fig. 6). Two cases can be distinguished.

In the first case a drift space is situated between the second and the third bump magnets. Using the Twiss form of transfer matrix, we obtain for the kick in the first bumper the expression

$$\varepsilon_1=\frac{X_s}{m_{12}^1}=\frac{X_s}{\sqrt{\beta_1\beta_2}\sin \mu_{12}}, \tag{2.2.2}$$

where we have denoted by M^1 the transfer matrix from BM_1 to BM_2 and by M^2 the transfer matrix from BM_1 to the septum. The kick in the second bumper must counteract the trajectory slope X':

$$\varepsilon_2=-X_2'=-m_{22}^1\varepsilon_1-\frac{X_s}{\beta_2}(\cot \mu_{12}-\alpha_2). \tag{2.2.3}$$

Finally, by symmetry,

$$\varepsilon_3=-\frac{X_s}{\beta_3}(\cot \mu_{34}-\alpha_3),$$

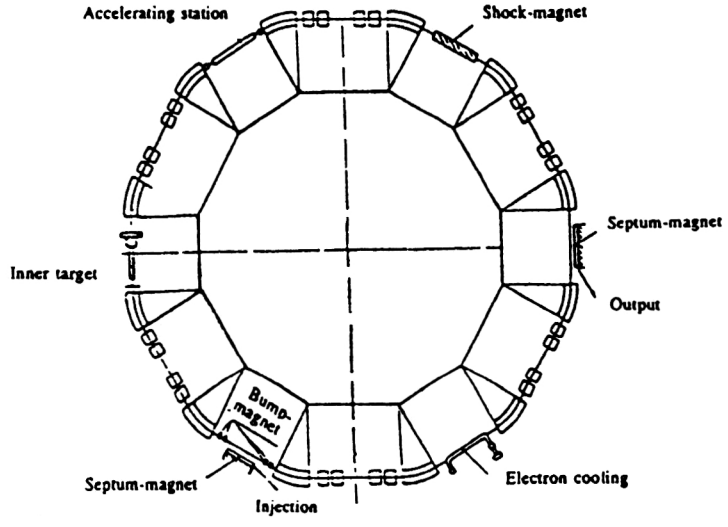

FIG. 2. The Nuclotron booster.[12]

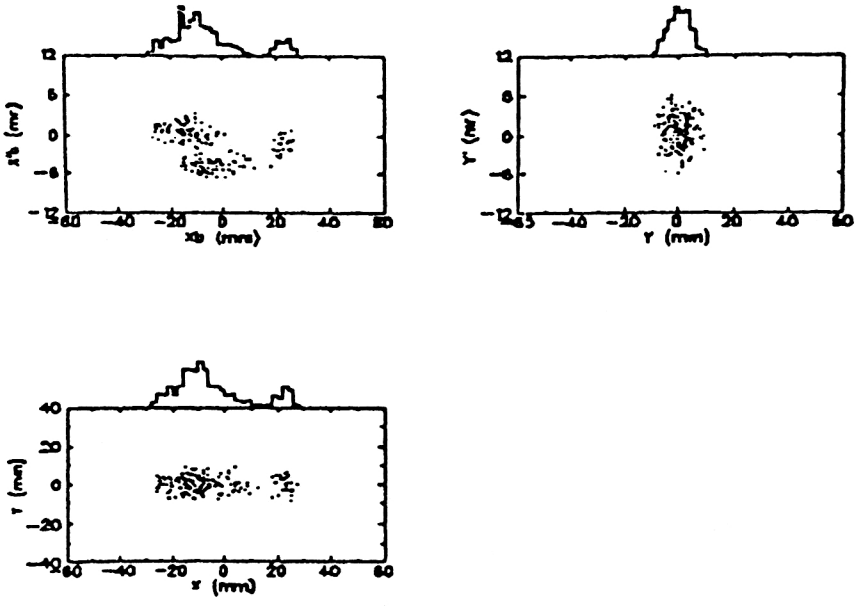

FIG. 3. Phase portrait of three-turn injection into the Nuclotron booster.[11]

$$\varepsilon_4=\frac{X_s}{\sqrt{\beta_3\beta_4}\sin\mu_{34}}. \tag{2.2.4}$$

In the second case, when no drift space but some elements (quadrupoles, for instance) lie between the second and the third bumper, it is still possible to obtain a zero slope at the injection azimuth, although the trajectory is more complicated.

For the strengths of the first two bump magnets one can deduce in this case

$$X_s=\sqrt{\beta_1\beta_s}\,\frac{\sin\mu_{12}}{(\cos\mu_{2s}-\alpha_s\sin\mu_{2s})}\,\varepsilon_1,$$

$$\varepsilon_2=-\sqrt{\frac{\beta_1}{\beta_2}}\,\frac{(\cos\mu_{1s}-\alpha_s\sin\mu_{1s})}{(\cos\mu_{2s}-\alpha_s\sin\mu_{2s})}\,\varepsilon_1. \tag{2.2.5}$$

By symmetry,

$$X_s=\sqrt{\beta_s\beta_4}\,\frac{\sin\mu_{34}}{(\cos\mu_{s3}-\alpha_s\sin\mu_{s3})}\,\varepsilon_4,$$

$$\varepsilon_3=-\sqrt{\frac{\beta_4}{\beta_3}}\,\frac{(\cos\mu_{s4}-\alpha_s\sin\mu_{s4})}{(\cos\mu_{s3}-\alpha_s\sin\mu_{s3})}\,\varepsilon_4. \tag{2.2.6}$$

2.3. Stacking efficiency

The injection efficiency is defined as the ratio of the accumulated beam current to the product of the injector current and the number of injection periods.

Different kinds of orbit bump falls—linear, exponential, cosine, etc.—can be applied. If the bump fall is exponential (Fig. 7), the number of accumulated particles increases faster, while the losses during the last periods are quite large because of the small orbit step. On the other hand, the cosine bump fall has larger losses during the first periods.

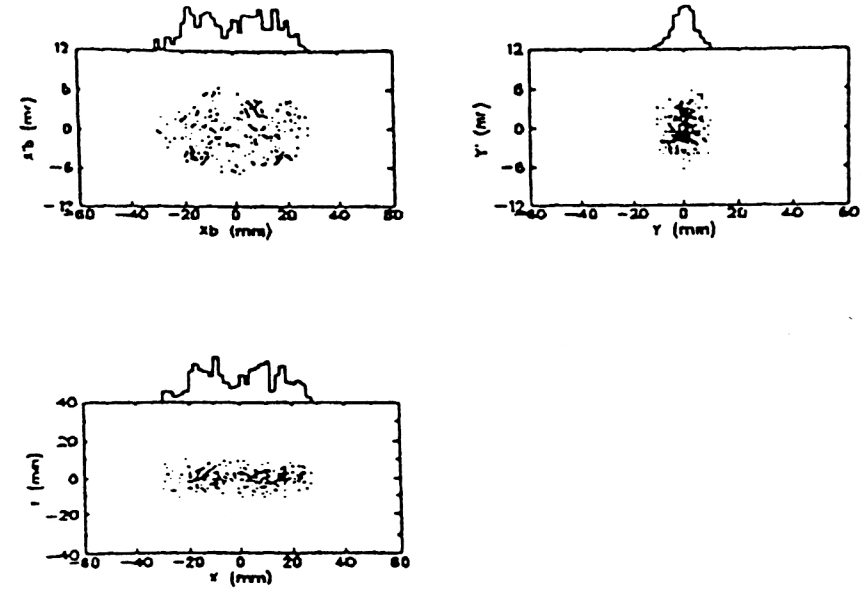

FIG. 4. Phase portrait of 15-turn injection into the Nuclotron booster.[11]

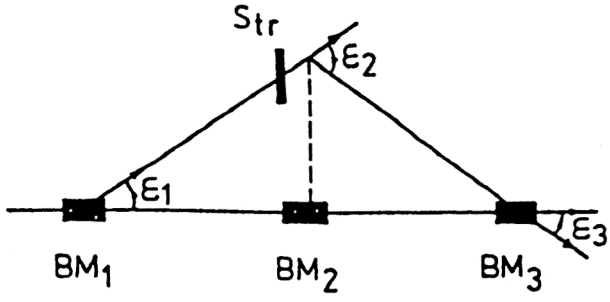

FIG. 5. Injection system with three bump magnets.

The stacking efficiency depends slightly on the law of bump fall (Fig. 8).

The stacking efficiency depends on a large number of parameters—the distance between beam center and septum, the slope of the injection beam, the number of injection periods (injection time), the number of betatron oscillations per turn Q, the injector emittance, the momentum spread in the injected beam, etc.

The curves for the efficiency versus the initial radial position of the injected beam X_0 and the efficiency versus the injected-beam slope X_0' have a resonant character (Figs. 9 and 10).

The dependence of the efficiency on the betatron number Q has a typical symmetrical shape (Fig. 11).

2.4. Improvements of the multiturn injection with betatron stacking

2.4.1. Multiturn injection with linear coupling

If both the horizontal and the vertical emittances of the injected beam are sufficiently smaller than the acceptance of the ring, one can realize multiturn injection with stacking in both the horizontal and vertical phase spaces by applying linear coupling of the betatron oscillations.[14,15]

Linear coupling occurs when $Q_x \approx Q_z$ in the presence of skew quadrupole or solenoidal magnetic fields. The strength of the coupling excited by skew quadrupole fields is determined by[16]

$$C_q=\frac{R}{2\pi Q}\frac{1}{B\rho}\oint\left\{\frac{dB_x}{dx}\right\}_{z=0}ds. \tag{2.4.1}$$

The linear coupling leads to beating of the horizontal and the vertical betatron oscillations. The amplitudes of the oscillations in the smooth approximation are

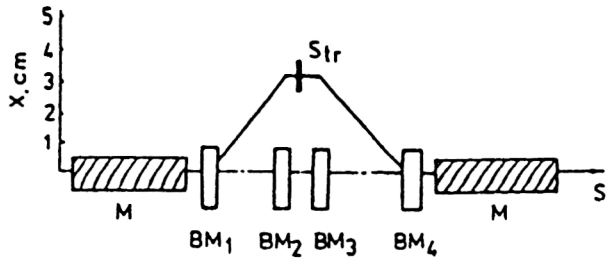

FIG. 6. Injection system with four bump magnets.

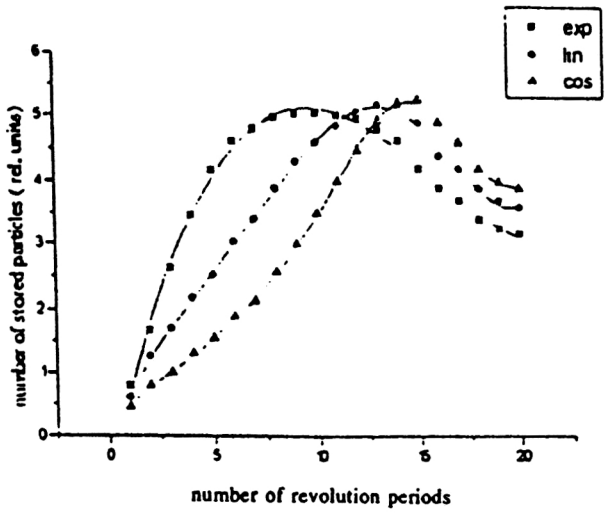

FIG. 7. Accumulation of particles in the Nuclotron booster during the multiturn injection for different laws of orbit bump fall.[11] Here N is the number of stored particles, and n is the number of injection turns. The injection covers 15 turns.

$$|X|^2=|A|^2+|B|^2\chi^2-2|AB^*|\chi\cos(Q_c\theta),$$
$$|Z|^2=|B|^2+|A|^2\chi^2+2|AB^*|\chi\cos(Q_c\theta), \tag{2.4.2}$$

where

$$\chi=\sqrt{1+\xi^2}-\xi, \tag{2.4.3}$$

$$\xi=\frac{B\rho Q\Delta}{R^2\left\langle\frac{dB_x}{dx}\right\rangle}, \tag{2.4.4}$$

$$\Delta=Q_x-Q_z, \tag{2.4.5}$$

$$Q=\frac{Q_x+Q_z}{2}. \tag{2.4.6}$$

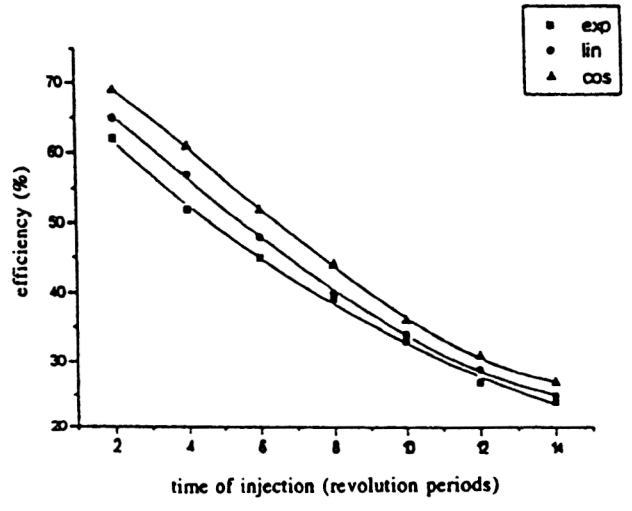

FIG. 8. Efficiency in the Nuclotron booster versus the number of injected turns for different laws of orbit bump fall.

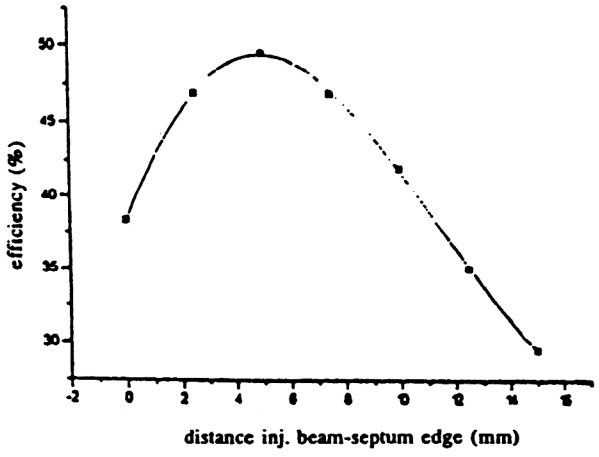

FIG. 9. Efficiency in the Nuclotron booster versus the distance between the injected-beam center and the septum.[11]

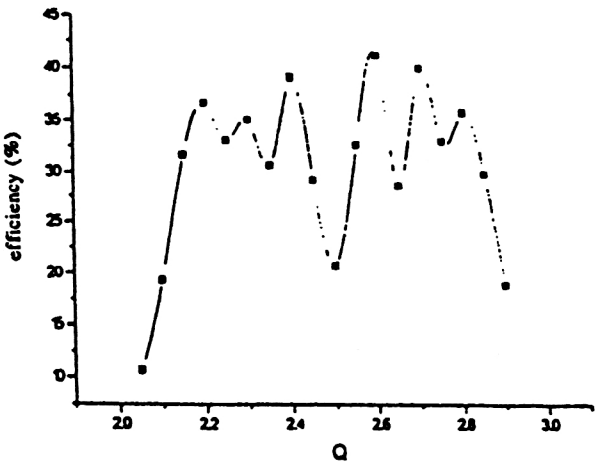

FIG. 11. Efficiency in the Nuclotron booster versus the betatron number Q.[11]

In (2.4.2), A and B are two complex constants of the motion, whose values are determined by the initial conditions, and Q_c is the beating wave number.

It can be shown that

$$Q_c=\sqrt{\Delta^2+C_q^2}. \tag{2.4.7}$$

According to (2.4.2), there is a sinusoidal exchange of energy from the horizontal to the vertical betatron oscillations and vice versa, while the total energy, i.e., $|X|^2+|Z|^2$, remains constant.

Thus, a beam injected in the medium plane close to the vacuum chamber wall will undergo horizontal betatron oscillations with decreasing amplitude. The energy of the horizontal oscillators goes to excite vertical betatron oscillators with increasing amplitude. After half of a beating period the beam will be extracted horizontally towards the machine center and vertically off the medium plane to the highest degree.

The strength of the amplitude modulation during the beating is given by

$$S=\frac{C_q}{\Delta^2+C_q^2}. \tag{2.4.8}$$

After that the process will return to small vertical and maximum horizontal amplitudes of the oscillations, which is why the injection process must be stopped.

As a result, we will have a phase-space portrait in both the horizontal and vertical planes.

Multiturn injection of heavy ions with linear coupling is realized, for instance, in the AGS booster.[17]

The injection is from a 1-MeV/u tandem Van de Graaff which delivers ion beams with very small transverse emittance. This allows very efficient multiturn injection (Fig. 12). The unperturbed values are: $Q_x=4.833$ and $Q_z=4.780$. A skew quadrupole induces significant $X-Z$ coupling during the injection. Typically, about 40 turns can be injected with an efficiency of 65%. By applying this scheme, the beam intensity has been increased by more than 50%.

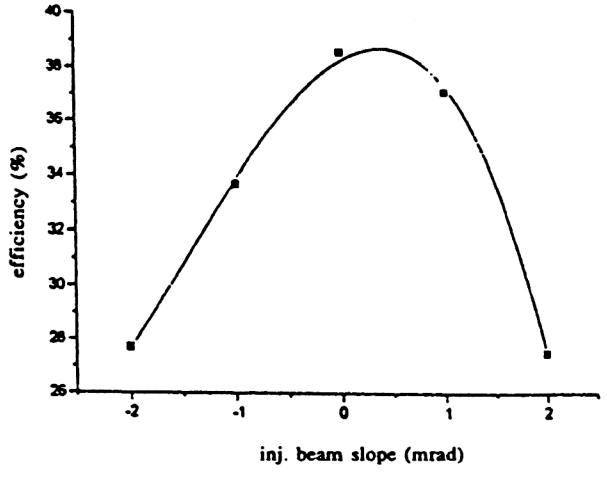

FIG. 10. Efficiency in the Nuclotron booster versus the injected-beam slope.[11]

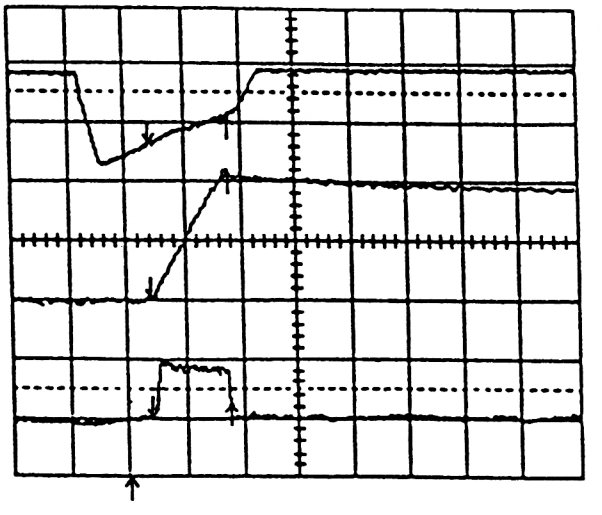

FIG. 12. Multiturn injection in the AGS booster. Oscilloscope traces of the injection kicker (top); circulating beam current (middle); beam pulse from the tandem (bottom). One horizontal box corresponds to 500 μs.[17]

2.4.2. Combination of multiturn injection with beam cooling

If the beam lifetime is long in comparison with the cooling time, it will be possible to combine electron cooling at injection energy with betatron stacking.

The cooler voltage is chosen so that the average ion momentum is not changed. During the cooling the beam shrinks transversely, and new injection pulses can be put next to the stack in the horizontal phase space. The injection consists in repetitive combinations of multiturn injection and successive electron cooling.

This type of injection is realized in the heavy-ion synchrotron SIS and in the cooler ring CRYRING.

In SIS the injection covers from 10 to 15 cycles within 1 s and allows the accumulation of $4 \cdot 10^9$ particles per pulse.[18] The cooling time for U^{79+} ions with energy 11.4 MeV/u is about 100 ms. The cooling reduces the beam emittance from 100 π mm·mrad down to 30 π mm·mrad. A series of ten repetitive multiturn injections with 80% efficiency will allow accumulation of $4 \cdot 10^9$ ions per pulse.

In CRYRING this combination is applied for the lightest fully stripped ions.[19] Thus, the lifetime of deuterons at 290 keV/u is 300 s. Provided that the betatron stacking–cooling process lasts 3 s, it will be possible to improve the stored intensity by a factor of 100. The real efficiency is smaller, as the stack of cooled ions occupies a part of the phase space where normally some of the injected pulses go. Nevertheless, 60 μA ($2 \cdot 10^9$ p) has been stored in the ring.

The accumulated intensity in the stacking–cooling process is limited by the space-charge effects (incoherent space-charge instabilities).

3. BEAM STACKING WITH rf ACCELERATION

3.1. Principle of rf stacking

Storage of the injected particles in the longitudinal phase space was first suggested by Symon and Sessler at MURA.[20] Later, this method was investigated experimentally in the model electron storage ring CESAR at CERN.[21] The method of rf stacking was used successfully for many years in the proton storage ring ISR at CERN.[22]

The principle of rf stacking[20–24] can be understood from Fig. 13, where a transverse cross section of the accelerator is shown.

The beam is injected by means of an electrostatic septum at position X_{inj}. After the injection of the first portion of the particles is completed, the stacking rf cavity is switched on and the particles are accelerated (or, more commonly, decelerated) to an outer (inner) orbit according to the relation

$$\frac{E}{R}\frac{dR}{dE} = \frac{\alpha}{\beta^2}, \tag{3.1.1}$$

where R is the physical radius of the machine, β is the relativistic factor, and α is the momentum compaction factor:[25,26]

$$\alpha = \frac{p}{R}\frac{dR}{dp} = \frac{\langle D_x \rangle_m}{R}. \tag{3.1.2}$$

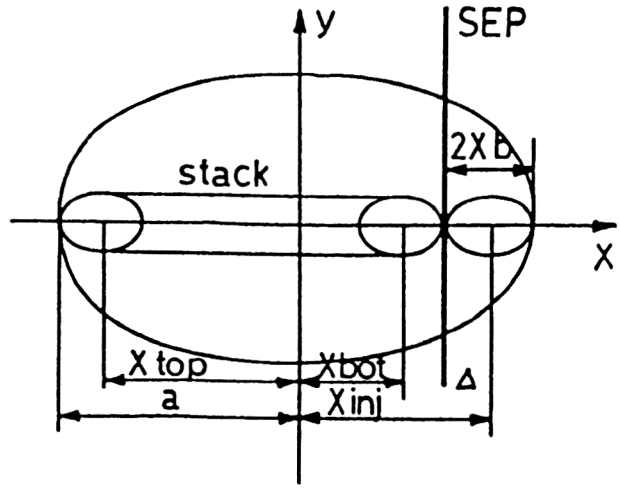

FIG. 13. Location of the injected and stacked beams in the accelerator aperture.

In (3.1.2), $\langle\ \rangle_m$ denotes averaging over the dipoles only, and D_x is the dispersion.

When the top of the stack is reached, the rf voltage is abruptly switched off and the particles are released from the rf buckets.

The rf cycle is then repeated, and the next injected portion is trapped in buckets and accelerated (decelerated).

There are two modes of operation.

In the so-called "repetitive-stacking" mode or "stacking at the top" the new portion is moved again to the same position, i.e., to the top of the stack. According to Liouville's theorem, the particle density in the longitudinal phase space must be conserved.[26] Hence the particles already accumulated in the stack will be displaced toward lower (higher) energies. Owing to the very small value of the momentum compaction factor (3.1.2) in the strong-focusing rings, the portions of the particles with different energies largely overlap in the physical and transverse phase spaces (Fig. 14). The stacking takes place in the longitudinal phase space, while the density in the 6-dimensional μ phase space is conserved, in agreement with Liouville's theorem. A beam stack with large intensity is built up.

In the "nonrepetitive-stacking" mode or "stacking at the bottom" each successive portion of the particles is moved to a slightly different energy from the previous one. The energy difference is equal to the final bucket area A_b divided by 2π. Thus, the new particles are added to the bottom of the stack.

3.2. Longitudinal phase-space topology

As was first shown by Symon and Sessler,[20] the equations of the longitudinal motion in an accelerator can be written in Hamiltonian form with the canonically conjugate variables

$$W = 2\pi \int_{E_0}^{E} \frac{dE}{\omega(E)} \tag{3.2.1}$$

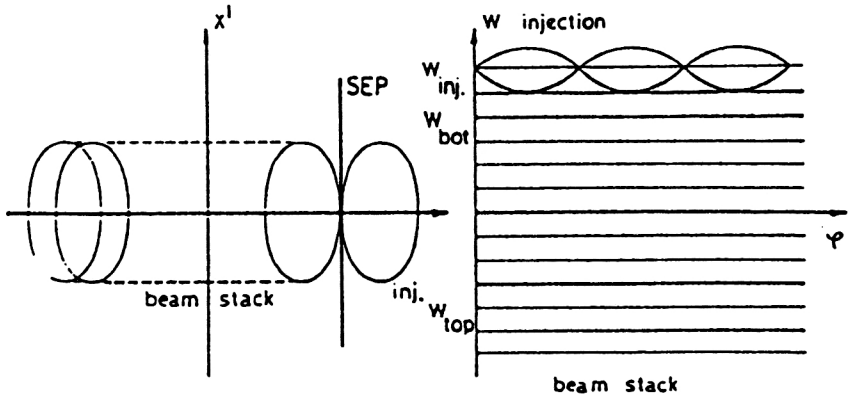

FIG. 14. Principle of rf stacking.

and the rf phase φ. In (3.2.1), $\omega(E)$ is the revolution frequency of a particle with energy E, and E_0 is an arbitrary energy.

The area of stable oscillations around the synchronous particle, the so-called rf bucket, is shown in Fig. 15 for the stationary case [$\Gamma=\sin\varphi_s=0$; no acceleration (deceleration)] and for moving buckets [$\Gamma=\sin\varphi_s\neq 0$; the particles are accelerated (decelerated)].

Let h be the harmonic number of the rf, so that we have h buckets simultaneously on the accelerator circumference. The area of these h buckets is as follows:

a) for stationary buckets,

$$A_{bs}=\frac{8\beta}{\omega_s}\sqrt{\frac{8\pi e\hat{V}E_s}{h|\eta|}}; \tag{3.2.2}$$

b) for moving buckets,

$$A_b=A_{bs}\alpha^*(\Gamma). \tag{3.2.3}$$

Here

$$\eta=\frac{p}{\omega}\frac{d\omega}{dp}=\frac{1}{\gamma^2}-\alpha=\frac{1}{\gamma^2}-\frac{1}{\gamma_{tr}^2}, \tag{3.2.4}$$

where γ is the relativistic factor and γ_{tr} is its value at the transition point. In (3.2.3), $\alpha^*(\Gamma)$ is a tabulated function of the synchronous phase $\Gamma=\sin\varphi_s$ (Fig. 16). In the rf stacking an important role is played by the Boltzmann–Ehrenfest adiabatic theorem,[26] which states that if the parameters (such as $\hat{V}$, φ_s, E_s, etc.) in the Hamiltonian H are varied sufficiently slowly, the particles lying on a closed curve $H(t_1)=\text{const}$ surrounding an area of stable oscillations A_1 at a time t_1 will remain on a closed curve $H(t_2)=\text{const}$ surrounding an area $A_2=A_1$ at a time $t_2>t_1$. Thus, the action integral $I=\oint W d\varphi$ is an invariant.

3.3. Stacking cycle

It is the phase-displacement phenomenon that underlies the rf stacking process. The phase displacement is a phenomenon related to the crossing of a coasting beam by an rf bucket (whether filled with particles or empty). The trajectories outside the separatrix are such that the particles will move in the direction opposite to that of the bucket (for an accelerating bucket to lower energy, and for a decelerating bucket to higher energy). According to Liouville's theorem,

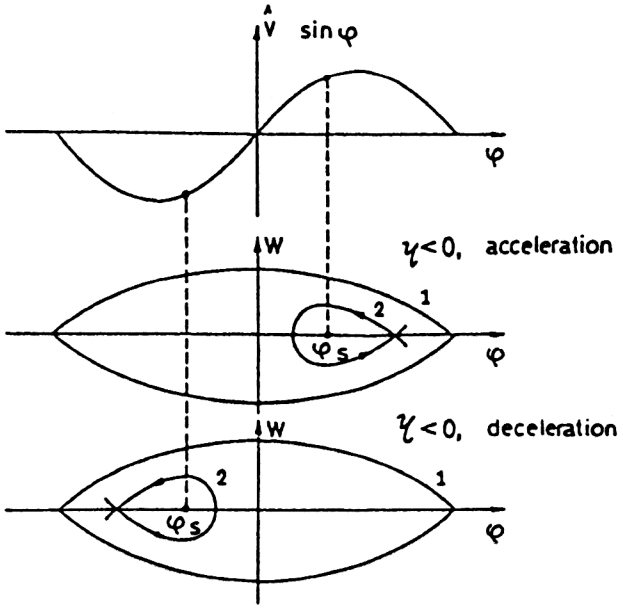

FIG. 15. Stationary and moving rf buckets.

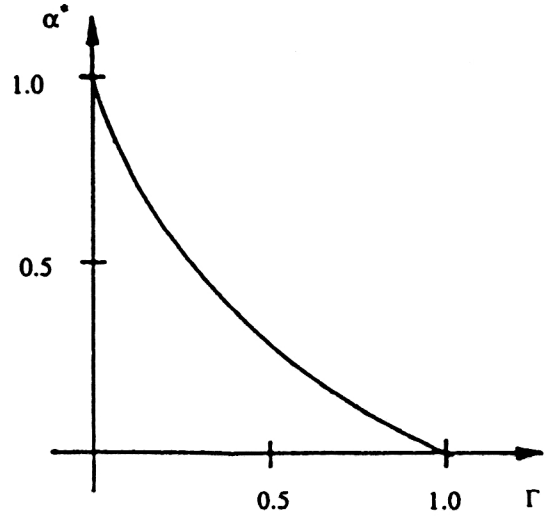

FIG. 16. The function $\alpha^*(\Gamma)$.

the area of the displacement of the coasting beam must be equal to the bucket area A_b. Hence the change in the mean energy of the coasting beam is

$$\Delta W = \frac{A_b}{2\pi}. \tag{3.3.1}$$

A detailed calculation of the change of the energy of a particle lying outside a moving bucket when this bucket crosses the particle was made in Refs. 27 and 28. It shows that the mean energy change obeys (3.3.1), while the energy spread in the coasting beam is increased.

Let us now examine the rf stacking cycle in more detail.

The stacking is performed at a constant magnetic field.

After the first portion of the particles is injected, it is immediately debunched, owing to the spread in the revolution frequency of particles having different energies.

The rf voltage is now switched on adiabatically, while the rf frequency is kept constant ($\varphi_s = 0$). The particles are trapped with high efficiency (more than 90%) in stationary buckets.

After the capture finishes, the rf buckets are decelerated toward the top of the stack.

As

$$\frac{E}{\omega}\frac{d\omega}{dE} = \frac{\eta}{\beta^2} \tag{3.3.2}$$

and

$$\frac{dE}{dt} = \frac{\omega}{2\pi} e\hat{V} \sin\varphi_s, \tag{3.3.3}$$

the rf frequency must be increased according to

$$\frac{d\omega_{\mathrm{rf}}}{dt} = \frac{\eta\omega_{\mathrm{rf}}^2}{2\pi h\beta^2 E} e\hat{V} \sin\varphi_s. \tag{3.3.4}$$

When ω_{rf} reaches the final frequency, the rf voltage is switched off, the bunches debunch, and a whole strip in the stack is populated with particles.

In the repetitive stacking mode each of the successive pulses crosses the whole stack and the particles are released at the top of the stack.

In each crossing the particles that are already stored are moved to higher energy by (3.3.1) according to the phase-displacement mechanism.

If the stack is built by n pulses, the ideal stack width will be

$$2\pi \frac{\Delta E_{\mathrm{ideal}}}{\omega} = n \frac{A_b}{2\pi}. \tag{3.3.5}$$

In fact, the particles will be distributed over a wider energy range $\Delta E_s > \Delta E_{\mathrm{ideal}}$.

In the nonrepetitive stacking mode the crossing of the whole stack by the buckets is avoided by successive reduction of the final rf frequency by an amount

$$\Delta\omega_{\mathrm{rf}} = \frac{\omega_{\mathrm{rf}}^2\eta}{\beta^2 E h}\frac{A_b}{(2\pi)^2}. \tag{3.3.6}$$

Thus, the particles will be deposited at the stack bottom.

It is natural to define the stacking efficiency as the ratio of the average phase-space density in the stack to that in the injected beam.[29]

The total stacking efficiency depends on two kinds of parameters:

$$\varepsilon_{\mathrm{tot}} = \varepsilon' \dot{\varepsilon}. \tag{3.3.7}$$

Here ε' describes the dependence of the stacking efficiency on the rf manipulation—mainly on the trapping efficiency in the buckets.

In (3.3.7), ε is the accumulation efficiency itself:

$$\varepsilon = \frac{N_{\mathrm{lim}}}{N_{\mathrm{tot}}}, \tag{3.3.8}$$

where N_{lim} is the number of particles in the ideal stack width and N_{tot} is the total number of particles in the stack. The parameter ε represents the reduction of the phase-space density due to the dilution of the stack by the moving rf buckets during the subsequent stacking cycles.

Experiments and computer simulations[29] show that ε is a function of the synchronous phase $\Gamma = \sin\varphi_s$ and of the number of stacking cycles n. There is an empirical formula

$$\varepsilon = \frac{1}{1 + \dfrac{2\Gamma}{3\sqrt{n}\alpha^*(\Gamma)}}, \tag{3.3.9}$$

which agrees quite well with the experimental results over a wide range of Γ and for not too small n.

As $\alpha^*(\Gamma)$ is a decreasing function of φ_s (Fig. 15), the stacking efficiency behaves as $\varepsilon \to 1$ when $\varphi_s \to 0$.

However, small values of φ_s will require very long stacking times according to (3.3.4), i.e., a compromise must be made.

3.4. Combination of multiturn injection and rf stacking

Both multiturn injection and rf stacking have their limits in the intensity of the accumulated beams. These limits have already been discussed above.

If we combine both accumulation mechanisms, much larger intensity multiplication factors can be realized. The stacking will take place in the 4-dimensional (x,x',W,φ) phase space. However, the physical aperture of the accelerator must be shared by the two methods. Let ε_0 be the area of the transverse phase plane (x,x') devoted to the multiturn injection. In order to estimate this area, a purely geometrical analysis can be carried out.[30]

From Fig. 13 one can easily deduce that the inequality

$$E_{\mathrm{inj}} - E_{\mathrm{top}} \leq 2E\beta^2\left(\frac{a - \sqrt{\varepsilon_0\beta(s)}}{D(s)}\right) \tag{3.4.1}$$

must be satisfied for any point s along the circumference, where $\beta(s)$ is the Twiss amplitude function and $D(s)$ is the dispersion.

On the other hand, at the injection point

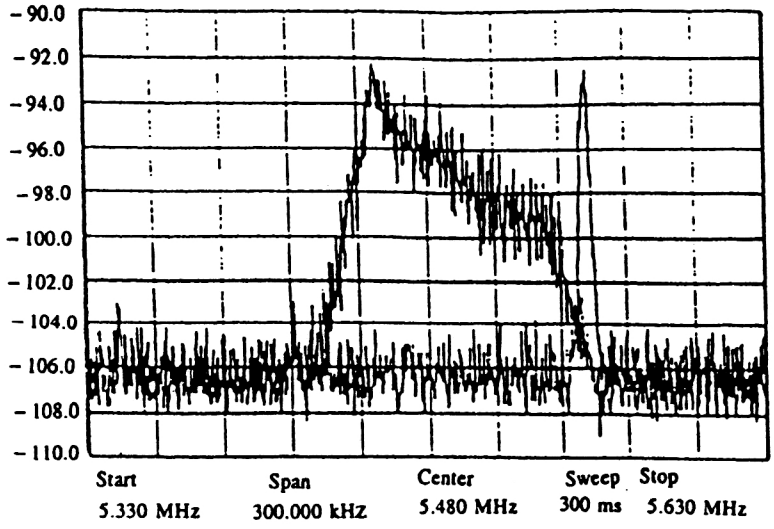

FIG. 17. TSR Schottky spectrum of the rf stack after accumulation of 30 cycles.[32]

$$E_{\text{inj}}-E_{\text{bot}}=E\beta^2\left(\frac{2\sqrt{\varepsilon_0\beta_{\text{inj}}}+\Delta}{D_{\text{inj}}}\right), \tag{3.4.2}$$

where Δ is the septum thickness.

Let S^* be the azimuth at which the right-hand side of (3.4.1) has a minimum, and let the corresponding values of $\beta(s)$ and $D(s)$ be β^* and D^*.

The number of rf cycles is

$$n_{\text{rf}}=\varepsilon_{\text{rf}}\frac{E_{\text{bot}}-E_{\text{top}}}{\Delta E}, \tag{3.4.3}$$

where ΔE is the phase displacement of the stack during a single crossing by the buckets [Eq. (3.3.1)] and ε_{rf} is the stacking efficiency, defined here as the ratio of the ideal stack width to the width of the real stack.[21]

The number of effective turns in the multiturn stage of the combined process is

$$n_m=\varepsilon_m\frac{\varepsilon_0}{\varepsilon_{\text{inj}}}, \tag{3.4.4}$$

where ε_{inj} is the emittance of the injected beam and ε_m is the multiturn injection efficiency.

Thus, the total number of effective turns will be

$$n_{\text{tot}}=n_m\cdot n_{\text{rf}}$$
$$=\varepsilon_m\varepsilon_{\text{rf}}\frac{E\beta^2}{\Delta E}\varepsilon_0\left[\frac{2(a-\sqrt{\varepsilon_0\beta^*})}{D^*}-\frac{2\sqrt{\varepsilon_0\beta_{\text{inj}}}+\Delta}{D_{\text{inj}}}\right]. \tag{3.4.5}$$

From (3.4.5) the optimum value of the phase area devoted especially to the multiturn injection can be calculated.

3.5. Examples of rf stacking

A. Heidelberg test storage ring (TSR)

The Heidelberg Heavy Ion Test Storage Ring (TSR)[31] is an experimental accelerator specially designed to investigate the electron cooling of heavy ions as well as the combined rf stacking scheme. The ring is able to store ions with energy up to 30 MeV/A (for $Z/A=0.5$) accelerated in an MP tandem–postaccelerator combination. The emittance of the injected particles is 1.5 π mm·rad, and the injected current is 9 μA.

A combined scheme of multiturn injection and rf stacking is used.[32] The phase area devoted to betatron stacking is $\varepsilon_0=96\pi$ mm·rad. It is filled for about 100 turns with an efficiency of 40%.

The repetitive-stacking mode is chosen for the rf stage of the accumulation process. The efficiency of the adiabatic capture of the ions in the buckets is 94%. The rf stacking involves 20 cycles, which gives a total number of effective turns $\eta_{\text{tot}}=800$. In fact, 7 mA (1.2×10^{10} ions) of C^{6+} ions with energy 6.1 MeV/A has been measured. The whole process takes about 12 ms.

Figure 17 shows the longitudinal Schottky spectrum of the rf stack after accumulation of 30 cycles.[32]

B. MIMAS booster–accumulator for SATURNE

MIMAS is a low-energy booster storage ring which accumulates heavy ions from a CRYEBIS (Dione)–RFQ combination at 187 keV/A and accelerates them to 11.9 MeV/A (for $Z/A=0.5$) for injection in the synchrotron SATURNE.[33] Dione generates ions in short 50-μs pulses at intervals of 20–50 ms.

In MIMAS, ions are stacked in the synchrotron phase space by a betatron deceleration scheme.[34] The deceleration voltage up to 500 V is made by flux variation in eight ion cores installed in one of the straight sections. Up to eight heavy-ion pulses can be injected and stored with a repetition rate of about 100 Hz.

The injection scheme can work with polarized protons and deuterons as well. The pulse produced by the ion source Hyperion is long (1 ms), with constant intensity, allowing for a constant filling of MIMAS.

With MIMAS the synchrotron SATURNE is capable of producing beams up to krypton at 700 MeV/A as well as high-intensity polarized protons and deuterons at 3 GeV.

4. CHARGE-EXCHANGE INJECTION

Charge-exchange injection is now the preferred injection method for proton machines, owing to its relative simplicity and a very high intensity of the stored beams.[35,36] Recently, this injection method has been successfully applied for light-ion storage in the CELSIUS[37] and COSY[38] cooler rings.

4.1. Principle of charge-exchange injection

The principle of charge-exchange injection consists in letting an injected beam pass through a thin internal foil.[36] Having passed through the foil, the ions change their charge, while the energy is practically unaltered and the beam rigidity $B\rho$ jumps to a new value according to the relation

$$B\rho=\frac{A}{300Z}\sqrt{T_n^2+2E_{0n}T_n}, \tag{4.1.1}$$

where $B\rho$ is in Tm; the kinetic energy T_n per nucleon is in MeV, and the rest of the energy per nucleon E_{0n} is also in MeV. This provides a spatial separation for the trajectories of the injected and circulating beams.

The charge-exchange process cannot be described by a Hamiltonian. That is why Liouville's theorem for phase-space density conservation does not work. This allows us to inject ions many times into one and the same area in the phase space, thus increasing the intensity of the stored beam (non-Liouville stacking).

4.2. Equilibrium charge-state distribution and equilibrium thickness of the stripping foil

As the beam ions travel through the matter, the relative content of ions in different charge states changes. The process is described by the following set of linear differential equations:

$$\frac{d\Phi_k}{dt}=\sum_j \Phi_j\sigma_{jk}, \tag{4.2.1}$$

where Φ_j is the percentage of the ions in the jth charge state in the beam; σ_{jk} is the cross section for the transition $j\rightarrow k$; t is the foil thickness in at/cm^2.

The charge-state distribution reaches equilibrium for sufficiently thick foils.[39,40] This equilibrium distribution, which is independent of the initial distribution in the beam, is determined only by the relations between different charge-exchange cross sections σ_{jk} and the ion velocity. The beam attains charge-state distribution equilibrium before a visible particle delay in the foil material is reached. The equilibrium distribution is the solution of the linear system

$$\sum_j \Phi_j\sigma_{jk}=0. \tag{4.2.2}$$

Thus, in order to calculate the equilibrium distribution and the equilibrium thickness, one needs the exact values of the electron loss and capture cross sections σ_{jk}. The first theoretical papers on the cross sections in ion–atom collisions were by N. Bohr. He found for the electron loss the expression[41]

$$\sigma_e\approx 4\pi a_0^2\frac{Z_t^2+Z_t}{q^2}\left(\frac{\beta_1}{\alpha}\right)^{-2}, \tag{4.2.3}$$

where $\alpha=1/137$ is the fine-structure constant and a_0 is the Bohr radius, while for electron capture (together with Lindhard) he found[42]

$$\sigma_c=\pi a_0^2 Z_t^{1/3}q^2\left(\frac{\beta_1}{\alpha}\right)^{-3}. \tag{4.2.4}$$

Unfortunately, experiments have shown that these formulas work well only over a quite narrow range of parameters. Many semi-empirical formulas for electron loss and capture cross sections have been put forward.[43–45]

For electron capture, experiments show that

$$\sigma_c\sim Z_{\rm pr}^{\alpha 1}V^{\alpha 2}Z_t^{\alpha 3}, \tag{4.2.5}$$

where

$$\alpha_1=4-5;\quad \alpha_2=(2-5);\quad \alpha_3=0.15-0.4.$$

The electron-loss cross section σ_e increases with target atomic number Z_t and decreases with projectile atomic number $Z_{\rm pr}[\sigma_e\sim Z_{\rm pr}^{\alpha}\alpha=-(1-3)]$, and depends strongly on the ion velocity. On the other hand, the experiments show that the cross sections for losses of more than one electron are not negligible. In this connection there was a proposal for a semi-empirical method[45] of calculating the cross sections for the loss of one or several electrons by fast multi-electron ions. Using this method, which is based on the results of an analysis of experimental data and theoretical calculations, the cross sections ($m=1-5$) have been obtained for the fast ions of iodine and uranium in nitrogen.

The problem is even more complicated, as the case of solid foils differs strongly from that of rare gases. While in rare gases the time between the successive ion–atom collisions is long enough for excited atoms to return to their ground state, in solid foils this time is short and the atomic state remains almost unchanged. This means that all the cross sections should be averaged over the excited states. For this reason the electron-loss cross sections in solids are larger than in gases, and the electron-capture cross sections are smaller. As a result, the equilibrium thicknesses in solid foils are larger (up to ten times) than those in gases.[46]

Accelerator experiments[47,48] show that for heavy ions with energies from 3.8 to 10.6 MeV/nucleon the equilibrium thickness of carbon foils lies between 250 and 350 μg/cm^2.

4.3. Equilibrium charge-state distributions behind the stripping foil

The equilibrium charge-state distributions of heavy-ion beams on traversing the stripping foil are represented by a Gaussian,[49] although the Gaussian describes continuous random variables, while the ion charge states q are discrete ones:

$$\Phi_q=\frac{1}{\sigma\sqrt{2\pi}}\,e^{-(q-\bar{q})/2\sigma^2}. \tag{4.3.1}$$

Equation (4.3.1) is valid if the average charge state $\bar{q}$ is not too close to Z_{pr}.

Several empirical formulas have been proposed for the average charge state $\bar{q}$. It is proposed to use the reduced velocity X as an independent variable in all these formulas:

$$X=\frac{V}{V'Z_{pr}^{0.45}}, \quad V'=3.6\times 10^8 \text{ cm/s}. \tag{4.3.2}$$

The Nikolaev–Dmitriev formula is[50]

$$\frac{\bar{q}}{Z_{pr}}=(1+X^{-1/0.6})^{-0.6}. \tag{4.3.3}$$

The To–Droin formula is[51]

$$\frac{\bar{q}}{Z_{pr}}=1-e^{-x}. \tag{4.3.4}$$

Shima's formulas are[52]

$$\frac{\bar{q}}{Z_{pr}}(Z_t=6)=1-\exp[-1.25X+0.32X^2-0.11X^3], \tag{4.3.5}$$

$$\frac{\bar{q}}{Z_{pr}}(Z_t\neq 6)=\frac{\bar{q}}{Z_{pr}}(Z_t=6)[1+g(Z_t)], \tag{4.3.6}$$

where

$$g(Z_t)=-0.0019(Z_t-6)\sqrt{X}+10^{-5}(Z_t-6)^2X. \tag{4.3.7}$$

The Heckman–Betz formula is[53–55]

$$\frac{\bar{q}}{Z}=1-C\exp\left(-\frac{V}{V_0Z_{pr}^{\gamma}}\right), \tag{4.3.8}$$

where C and γ are constants depending on Z_{pr} in the intervals $C\in(1.07-1.25)$ and $\gamma\in(0.57-0.65)$, and $v_0/c=137$. The Baron–Ricaud formula is[47]

$$\frac{\bar{q}}{Z}=1-C\exp\left(-\frac{83.275\beta}{Z^{0.447}}\right), \tag{4.3.9}$$

where $C=\begin{cases}1, & \text{for } T_{pr}>1 \text{ MeV/n},\\ 0.9+0.0769\ T_{pr}, & \text{for } T_{pr}<1 \text{ MeV/n}.\end{cases}$

Equations (4.3.1)–(4.3.5) have been deduced by scaling experimental data over an energy range below 2 MeV/n. Equation (4.3.3) scales the experimental data over a wider energy range up to $X=2.5$ and also describes the cases of non-carbon foils. In Ref. 47 the following correction for heavier ions ($Z\geqslant 54$) has been deduced:

$$\bar{q}_p=\bar{q}_p[1-\exp(-12.905+0.2124Z-0.00122Z^2)], \tag{4.3.10}$$

where $\bar{q}_p$ is taken from (4.3.9).

For the standard deviation Nikolaev and Dmitriev[50] propose the following expression:

$$\sigma=0.5\sqrt{\bar{q}\left(1-\left(\frac{q}{Z}\right)^{1.67}\right)}. \tag{4.3.11}$$

The following correction for heavier ions ($Z\geqslant 54$) is proposed in Ref. 47:

TABLE III. Ar_{40}^{6+}, $T_n=5.62$ MeV/n.

d, μg/cm^2	q				
	14	15	16	17	18
60	1.76	13.69	45.40	32.39	6.74
84	1.26	10.57	39.64	37.86	10.58
120	0.96	8.17	35.11	40.54	14.92
150	0.85	7.95	32.47	42.26	16.78
215	0.55	5.53	26.55	43.79	23.59
300	0.04	3.81	25.10	45.21	25.25

$$\sigma=\sqrt{\bar{q}_p(0.07535+0.19Y-0.2654Y^2)}, \quad Y=\frac{\bar{q}_p}{Z}. \tag{4.3.12}$$

Some experimental data for the charge distribution of Ar ions behind carbon foils of different thicknesses and energy 5.62 MeV/n are presented in Table III.[47]

4.4. Heavy-ion scattering in the stripping foil

The Coulomb elastic scattering of beam ions in a stripping foil will cause a change of the trajectory slopes.

The mean energy loss of an ion per unit path length when $m_{pr}\leqslant 0.2m_t$, where m_{pr} is the particle mass and m_t is the target-nucleus mass, is given by[56]

$$\left(-\frac{dE}{dx}\right)_{0l}=\frac{2\pi Z_{pr}^2Z_t^2e^4nm_{pr}}{m_tE_{pr}}\left\{\ln\sin\frac{\theta_{min}}{2}+\frac{1}{2}\frac{m_t^2-m_{pr}m_t-m_{pr}^2}{(m_{pr}+m_t)^2}\right\}. \tag{4.4.1}$$

In (4.4.1), n denotes the number of target atoms per unit volume and E_{pr} is the particle energy.

It can be shown[56] that the ratio of the ionization losses and Coulomb-scattering energy losses is

$$\frac{\left(-\frac{dE}{dx}\right)_{ion}}{\left(-\frac{dE}{dx}\right)_{sct}}=\frac{1}{\left(\frac{m_0Z_t}{A_tm_p}\right)}\approx 4000, \tag{4.4.2}$$

where m_p is the proton rest mass and A_t is the atomic weight of the target material.

From (4.4.2) it follows that the energy losses in Coulomb scattering are negligible.

On the other hand, the particle-trajectory changes are very important.

The basic laws of elastic Coulomb scattering have been well known since the time of Rutherford's pioneering work.

An important role in accelerator practice is played by multiple scattering in the foil material.

It can be shown that the multiple-scattering mean-square angle is[56]

$$\langle\theta^2\rangle=0.078\frac{Z_{pr}^2Z_t^2t}{E_{pr}^2A_t}\ln\left\{1.06\times 10^2\frac{Z_{pr}Z_t^{1/3}}{\beta_{pr}}\sqrt{\frac{t}{A_t}}\right\}, \tag{4.4.3}$$

where E_{pr} is the particle kinetic energy in MeV and t is the target thickness in g/cm^2.

In Ref. 59 the following empirical formula for the multiple-scattering mean-square angle of heavy ions in solid foils is given:

$$\langle \vartheta^2 \rangle = 0.250 \frac{Z_t(Z_t+1)}{A_t} \frac{Z_{pr}^2}{E_{pr}^2} t, \tag{4.4.4}$$

where ϑ is in mrad; the stripper thickness t is in μg/cm^2, and the particle energy E_{pr} is in MeV.

The average number of scatterings per particle and passage is

$$n_{sct} = 0.0392 \frac{Z_{pr}^2 Z_t^2 \gamma_{pr}^t}{A_t E_{pr}^2} \frac{1}{\vartheta_\alpha}. \tag{4.4.5}$$

Here ϑ_α is the so-called screening angle, given by

$$\vartheta_\alpha = 4.52\times 10^{-3} \sqrt{1.78\times 10^{-4} Z_{pr}^2 Z_t^2 + \beta_{pr}^2} \frac{\sqrt[3]{Z_t}}{E_{pr}\beta_{pr}^2\gamma_{pr}}, \tag{4.4.6}$$

where t is the target thickness in g/cm^2, E_{pr} is the projectile energy in MeV, and E_0 is the particle energy in MeV.

4.5. Emittance growth due to elastic Coulomb scattering in the stripping foil

It is convenient to work in the normalized phase space (y,y^*), where y is the transverse coordinate (either X or Z) and

$$y^* = \alpha y + \beta y'. \tag{4.5.1}$$

In (4.5.1), α and β are the Twiss functions and the prime denotes differentiation with respect to the longitudinal coordinate S.

In the normalized phase space the betatron oscillations can be represented in the form

$$y = A\cos(\psi+\alpha),$$
$$y^* = A\sin(\psi+\alpha), \tag{4.5.2}$$

where ψ is the betatron phase, $\psi = \int ds/\beta(s)$, and A and α are constants.

Let y and y^* be Gaussian distributions. The betatron amplitude is

$$A^2 = y^2 + y^{*2}. \tag{4.5.3}$$

The relation (4.5.3) defines a circle in the normalized phase space with radius A. In order to find the amplitude distribution, we must integrate the joint probability distribution around this circle. In polar coordinates,

$$P(A) = \int_0^{2\pi} p(y,y^*) A d\varphi = \int_0^{2\pi} \frac{A}{2\pi\sigma^2} e^{-A^2/2\pi\sigma^2} d\varphi$$
$$= \frac{A}{\sigma^2} e^{-A^2/2\pi\sigma^2}, \tag{4.5.4}$$

i.e., we have obtained a Rayleigh distribution with

$$\sigma^2 = 2\sigma_y^2. \tag{4.5.5}$$

In passing through the stripper the beam particles change by a jump in the slope of their trajectory, with no change in the distance from the equilibrium orbit:

$$y = y_0, \quad y^* = y_0^* + \Delta y^* = y_0^* + \beta \Delta y'. \tag{4.5.6}$$

Behind the stripper we have

$$A^2 = A_0^2 + 2\Delta y^* y_0^* + \Delta y^{*2}. \tag{4.5.7}$$

Averaging (4.5.7), we obtain

$$\sigma_A^2 = \sigma_{A0}^2 + \sigma_{\Delta y^*}^2 = \sigma_{A0}^2 + \beta^2 \sigma_{0\Delta y'}^2. \tag{4.5.8}$$

However, the real situation in charge-exchange injection is more complicated. At the end of the injection process we have on the accelerator circumference simultaneously particles passing N times through the stripper, particles passing $N-1$ times, and so on, up to particles having crossed the stripper only once.

Obviously, in this case the probability for an amplitude is the normalized sum of the probabilities for the amplitudes after different numbers of foil crossings:

$$p(A) = \frac{1}{N} \sum_{i=1}^{N} p_i(A). \tag{4.5.9}$$

Then

$$\sigma_A^2 = \frac{1}{N} \sum_{i=1}^{N} \sigma_{Ai}^2 \tag{4.5.10}$$

but

$$\sigma_{Ai}^2 = \sigma_{A0}^2 + \beta_0^2 \sigma_{\Delta y'}^2. \tag{4.5.11}$$

Thus, we obtain

$$\sigma_A^2 = \sigma_{A0}^2 + \frac{N+1}{2} \beta_0^2 \sigma_{\Delta y'}^2. \tag{4.5.12}$$

From (4.5.12) we can deduce the emittance growth due to elastic Coulomb scattering:

$$\varepsilon_N = \frac{\sigma^2 A}{\beta_0} \simeq \varepsilon_0 + \frac{1}{2} N\beta_0 \langle \vartheta^2 \rangle. \tag{4.5.13}$$

4.6. Energy losses in the stripping foil

The energy losses of beam particles in the stripping foil are mainly due to the excitation and ionization of foil atoms.

The mean losses are described by the well-known Bethe–Bloch formula[56–58]

$$\frac{dE}{dx} = \frac{DZ_t\rho_t}{A_t} \left(\frac{Z_{pr}}{\beta}\right)^2 \left[\ln\left(\frac{2m_e\gamma^2\beta^2c^2}{I}\right) - \beta^2 - \frac{\delta}{2} - \frac{e}{Z_t}\right]$$
$$\times (1+\nu), \tag{4.6.1}$$

where ρ is the mass foil density,

$$D = 4\pi N_A r_e m_e e^2 = 0.3070 \text{ MeV}\cdot\text{cm}^2/\text{g},$$

and I is the mean ionization potential of the atoms of the medium:

$$I \approx 13.5 Z_t, \text{ eV}; \tag{4.6.2}$$

δ, c, ν are phenomenological functions, whose values are usually negligibly small; δ represents the density effect, and c represents shell corrections.

4.7. Emittance growth due to the energy losses

If the dispersion in the stripper is nonzero, then the energy losses will cause emittance growth according to the well-known relations

$$\Delta y = -D_0 \frac{\Delta p}{p},$$

$$\Delta y' = -D_0' \frac{\Delta p}{p}, \tag{4.7.1}$$

where D_0 and D_0' are the linear and angular dispersions in the stripper and $\Delta p/p$ is related to the energy losses by

$$\frac{\Delta E}{E} = \beta^2 \frac{\Delta p}{p}, \tag{4.7.2}$$

where E is the total particle energy.

The minus sign in (4.7.1) implies that in traversing the foil the particles remain in the same position, while because of the energy losses the corresponding off-momentum equilibrium orbit jumps to a new position. We will perform our analysis in the normalized phase space (y, y^*), where betatron oscillations are represented by circles. From a simple geometrical analysis one can deduce that

$$\sqrt{\beta_0 \varepsilon} = \sqrt{\beta_0 \varepsilon_0} + k\sqrt{\Delta y^2 + \Delta y^{*2}}, \tag{4.7.3}$$

where ε_0 is the initial emittance, ε is a new emittance, and k is the number of turns.

4.8. Ionization losses straggling in the stripping foil

The maximum energy transferrable by a fast-moving charged particle to an electron is[60]

$$E_{\max} = \frac{2m_e \beta_{\rm pr}^2 \gamma_{\rm pr}^2 c^2}{1 + 2\gamma\left(\frac{m_e}{m_{\rm pr}}\right) + \left(\frac{m_e}{m_{\rm pr}}\right)^2}. \tag{4.8.1}$$

In our case, $E_{\max} = 10.22$ keV.

The ionization losses are statistical in nature. There exists a probability distribution function $f(x,\Delta)$, so that $f(x,\Delta)d\Delta$ is the probability that an ion, on traversing a path length x in the target, will suffer an energy loss between Δ and $\Delta + d\Delta$.

The character of the distribution function depends on the parameter κ:[62]

$$\kappa = \frac{\xi}{E_{\max}}, \tag{4.8.2}$$

where

$$\xi = \frac{2\pi n e^4 Z_{\rm pr.\,eff}^2 Z X_t}{m_e \nu_{\rm pr}^2}, \tag{4.8.3}$$

n is the number of target atoms per unit volume, X is the target thickness, and $Z_{\rm pr.\,eff}$ is the ion effective charge:

$$Z_{\rm eff} = Z\left[1 - \exp\left(-0.95 \frac{\nu h}{e^2 Z^{2/9}}\right)\right]$$

$$= Z[1 - \exp(-130\beta Z^{-2/9})]. \tag{4.8.4}$$

a) If $\kappa < 0.05$, the distribution is highly asymmetric with respect to a long tail, and we have the so-called Landau distribution[61]

$$f(x,\Delta) = \frac{1}{\xi}\varphi(\lambda), \tag{4.8.5}$$

$$\varphi(\lambda) = \frac{1}{2\pi i}\int_{\sigma - i\infty}^{\sigma + i\infty} e^{u \ln u + \lambda u} du,$$

$$\lambda = \frac{\Delta - \xi\left(\ln\frac{\xi}{\xi'} + 1 - c\right)}{\xi},$$

where c is Euler's constant $c = 0.5777\ldots$, and

$$\ln \varepsilon' = \ln\left[\frac{(1-\beta^2)I^2}{m\nu^2}\right] + \beta^2. \tag{4.8.6}$$

b) If $0.05 < \kappa < 10$, we have the case of Vavilov's distribution[62]

$$f(x,\Delta) = \frac{1}{\pi\xi}\kappa e^{\kappa(1+\beta^2 c)}\int_0^\infty e^{\kappa f_1}\cos(y f_1 + \kappa f_2) dy, \tag{4.8.7}$$

$$f_1 = \beta^2(\ln y - \mathrm{Ci}(y)) - \cos y - y\,\mathrm{Si}(y),$$

$$f_2 = y(\ln y - \mathrm{Ci}(y)) + \sin y + \beta^2\,\mathrm{Si}(y),$$

where Si and Ci are the sin and cos integrals.

c) If $\kappa > 10$, the distribution is Gaussian:

$$f(x,\Delta) = \frac{1}{\sqrt{2\pi\gamma x}} e^{-(\Delta - \alpha x)^2/2\gamma x}, \tag{4.8.8}$$

where, according to Landau's notation,

$$\alpha \equiv \langle\Delta\rangle = \int_0^\infty \varepsilon w(\varepsilon) d\varepsilon \tag{4.8.9}$$

and

$$\gamma = \int_0^{\varepsilon_{\max}} \varepsilon^2 w(\varepsilon) d\varepsilon = \frac{\xi}{x}\varepsilon_{\max}\left(1 - \tfrac{1}{2}\beta^2\right) \tag{4.8.10}$$

are the mean and variance for unit path length.

The situation with regard to charge-exchange injection is a little more complicated because we have simultaneously on the orbit particles traversing the foil N times, $N-1$ times, etc., up to one time. Then the common probability density is

$$p(\Delta) = \frac{1}{N}\sum_{i=1}^{N} p_i(\Delta), \tag{4.8.11}$$

where $p_i(\Delta)$ is the probability density for particles traversing the foil ith times.

From (4.8.11), and taking into account the large value of N, one can deduce for the energy dispersion in a stored beam the expression

$$\sigma_N^2=\sigma_0^2+\frac{N}{2}\sigma_t^2+\frac{N^2}{12}\langle\Delta\rangle_t^2, \tag{4.8.12}$$

where σ_0^2 is the energy dispersion in the incident beam, σ_t^2 is the dispersion of ionization losses in the foil material (one passage through the target), and $\langle\Delta\rangle_t$ are the mean ionization losses in the foil.

4.9. Ion storage—fixed-orbit bump mode

In this mode the orbit bump remains unchanged. Ions pass through the stripper many times until an equilibrium is attained or until other limited factors—scattering and energy losses—begin to restrict the number of stored particles.

The storage process can be described in the following way.

a) During the first turn the number of stored particles increases as $N_t=\Delta I t$, where $\Delta I=I_0\sigma_1 nt$ is the ion current behind the target, I_0 is the injected-beam current, σ_1 is the circulating charge ($Z_c\approx q$) formation cross section, n is the number of target atoms per unit volume, and t is the target thickness. At the end of the first turn we have $N_t=\Delta I\cdot T$ particles on the orbit, where T is the period of the synchronous particle.

b) During the second turn the circulating particles pass through the target for the second time. Let σ_2 be the circulating-charge formation cross section for the circulating particles. Generally speaking, $\sigma_2\neq\sigma_1$, as the charge-state distribution in the injected beam differs from that in the circulating beam. If the former is centered on charge number $Z_0\neq Z_c$ (otherwise, charge-exchange injection will not work), the circulating beam contains only ions in one charge state. Ions in other charge states have already been lost on the walls of the vacuum chamber because for them $\Delta Z/Z_c$ is quite large. Simultaneously new particles are injected into the ring, and these particles pass through the stripping foil only once. Summarizing, we can obtain for the number of the stored particles the expression

$$N_t=\Delta I(t-T)+\sigma_2 nt\Delta I(t-T)+\Delta I(2T-t) \tag{4.9.1}$$

and, at the end of the second turn,

$$N_{2T}=\Delta I(1+\sigma_2 nt)T. \tag{4.9.2}$$

Following this reasoning, we can obtain for the kth turn $N_t=\Delta I(1+b+\ldots+b^{k-1})T$, where $b=\sigma_2 nt$. Summing the geometrical progression in the brackets, we get

$$N_k=N_\infty(1-b^k), \tag{4.9.3}$$

where

$$N_\infty=\left(\frac{a}{1-b}\right)I_0T,\quad a=\sigma_1 nt,\quad b=\sigma_2 nt, \tag{4.9.4}$$

in which T is the period of the synchronous particle; I_0 is the injected current, σ_1 is the cross section for the formation of ions with equilibrium charge from the injected ions, and σ_2 is the cross section for the formation of ions with equilibrium charge from the circulating ions.

In the specific case of a stripping target with equilibrium thickness, the charge-state distribution behind the target will reach equilibrium, which means that it is independent of the charge distribution in the incident beam and that it will no longer change. For the target of equilibrium thickness, $\sigma_1 nt=\sigma_2 nt=\Phi_{zc}$, i.e., the probability of circulating charge formation for the injected beam is equal to that for the circulating beam. Equation (4.9.4) then becomes simpler:

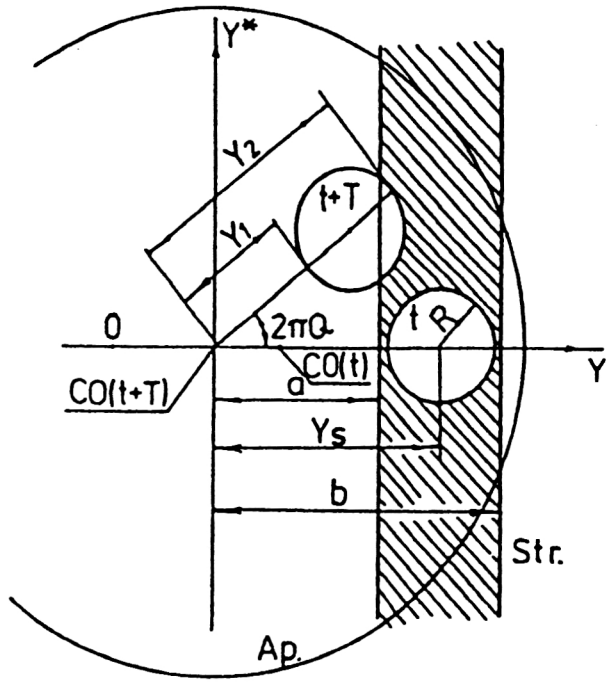

FIG. 18. Charge-exchange injection with a moving orbit bump.

$$N_k=N_\infty(1-\Phi_{zc}^k), \tag{4.9.5}$$

$$N_\infty=\left(\frac{k}{1-\Phi_{zc}}\right)I_0T. \tag{4.9.6}$$

4.10. Ion storage—moving orbit bump mode

In this mode the orbit bump is gradually reduced to zero during the injection.

When the orbit is close to the center of the stripper, the injected particles cross it during every turn. On the other hand, the particles injected when the orbit lies outside the stripper undergo betatron oscillations and avoid the stripper during most of the turns. In other words, we have a kind of combination between multiturn and stripping injections. Such a combination allows the number of injection turns to be increased many times.

The goal of this section is to estimate the total number of injected particles in the mode under consideration. We will use a beam model with a uniform charge distribution and clear-cut boundaries which are circles in the normalized phase space. Let us consider a beam slice $dN=I_0 dt$ injected at time t (Fig. 18). After one turn the slice occupies a position forming an angle $\alpha=2\pi Q$ with the initial position, as depicted in Fig. 18.

Let us denote the beam radius by $R=\sqrt{\beta_0\varepsilon}$ and the aperture radius by A. As $A\gg R$, we will approximate the aper-

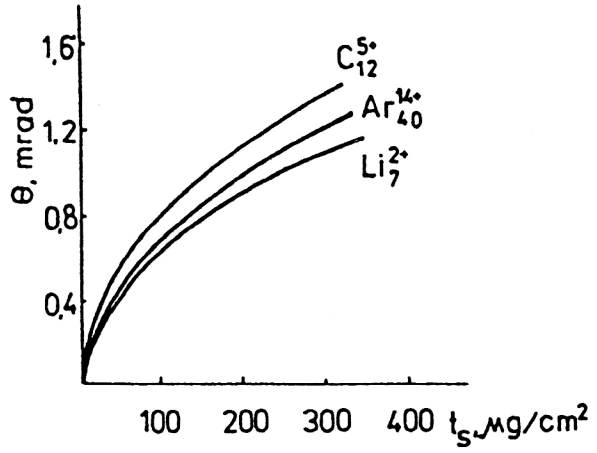

FIG. 19. Multiple-scattering rms angle for charge-exchange injection into the Nuclotron booster.[63]

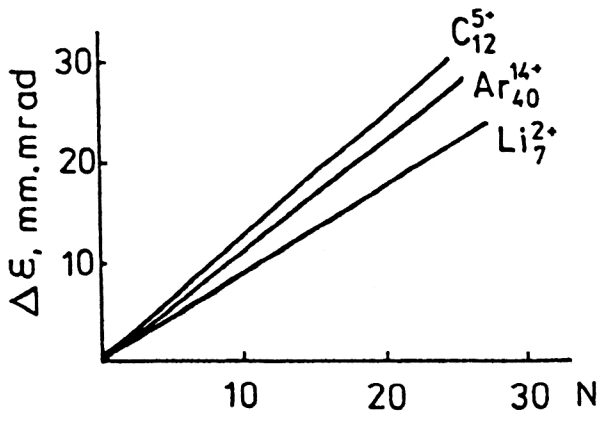

FIG. 20. Emittance growth in the Nuclotron booster due to multiple scattering; the target thickness is 100 μg/cm^2, and $\beta_0=4.5$ m.[63]

ture boundary lying within the slice by a straight line, so that the part of the slice outside the aperture will be approximated by a segment of a circle.

Under these assumptions a purely geometrical analysis can be carried out. From Fig. 1 we find that

$$y_1(t)=y_s-R-y_{c0}(t),$$
$$y_2(t)=y_s+R-y_{c0}(t). \tag{4.10.1}$$

For the extreme left (y') and extreme right (y'') projections of the slice on the y axis we have

$$y'(t+jT)=y_{c0}(t+jT)+y_1\cos j2\pi Q - R(1-\cos j2\pi Q),$$
$$y''(t+jT)=y_{c0}(t+jT)+y_2\cos j2\pi Q + R(1-\cos j2\pi Q),$$
$$j=0,1,2,\ldots . \tag{4.10.2}$$

The stripper edge cuts a segment of a circle with area S_1 from the beam slice. If H is the distance from the edge to the slice center, we can write

$$H(t+jT)=a-y_{c0}(t+jT)-(y_s-y_{c0}(t))\cos j2\pi Q \tag{4.10.3}$$

and

$$S_1(t+jT)=R^2\arccos\left(\frac{H}{R}\right)-H\sqrt{R^2-H^2},$$
$$j=0,1,2,\ldots . \tag{4.10.4}$$

Another kind of restriction comes from the machine aperture. The aperture is centered on the instantaneous closed-orbit position. This means that at the beginning of injection, when the orbit bump passes through the stripper, we have no aperture limitations. However, when the orbit bump is small enough to go close to the machine center, there are strong aperture restrictions on the beam. The closer the orbit passes to the machine center, the stronger the aperture restrictions will be.

As mentioned above, we will assume that the aperture also cuts a segment of a circle (with area S_c) from the beam slice. This approximation improves as A becomes larger than R. By analogy with (4.10.4) we can deduce that

$$S_c^2(t)=R\arccos\left(\frac{H_c}{R}\right)-H_c\sqrt{R^2-H_c^2}, \tag{4.10.5}$$

where

$$H_c(t)=y_{c0}(t)+A-y_s \tag{4.10.6}$$

is the distance between the aperture edge and the slice center.

The main parameter of our analysis is the transition coefficient k, the percentage of particles having passed through the stripper and accepted in the aperture.

It can be shown that

$$k(t+jT)=\begin{cases}\Phi, & a<y'(t+jT),\quad R\leq H_0(t),\\ \dfrac{\pi R-S_c(t)}{\pi R^2}\Phi, & a\leq y'(t+jT),\\ & H_c(t)<R,\\ \dfrac{\pi R^2-(1-\Phi)S_1(t+jT)}{\pi R^2}, & \\ & y'(t+jT)<a<y''(t+jT),\\ & H_c(t)\geq R,\\ \dfrac{\pi R^2-(1-\Phi)S_1(t+jT)-\Phi S_c(t)}{\pi R^2}, & \\ & y'(t+jT)<a<y''(t+jT),\\ & H_c(t)\geq H(t+jT),\\ \dfrac{\pi R^2-S_c(t)}{\pi R^2}, & y'(t+jT)<a<y''(t+jT),\\ & H_c(t)<H(t+jT),\\ 1, & y''(t+jT)<a,\quad H_c(t)\geq R,\\ \dfrac{\pi R^2-S_c(t)}{\pi R^2}, & y''(t+jT)<a,\quad H_c(t)<R,\end{cases} \tag{4.10.7}$$

$(j=0,\ 1,\ 2,\ldots)$

where

$$\Phi=\begin{cases}\sigma_1 nt, & \text{for the injected beam,}\\ \sigma_2 nt, & \text{for the circulating beam,}\end{cases} \tag{4.10.8}$$

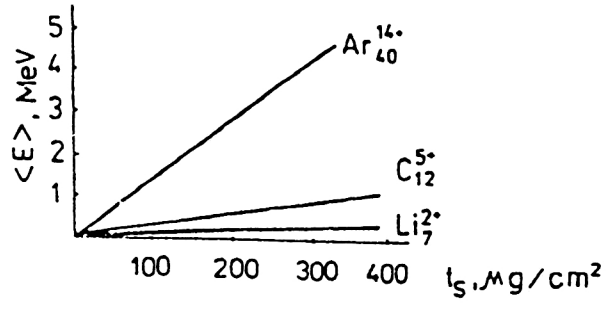

FIG. 21. Energy losses in the Nuclotron-booster carbon stripping foil.[63]

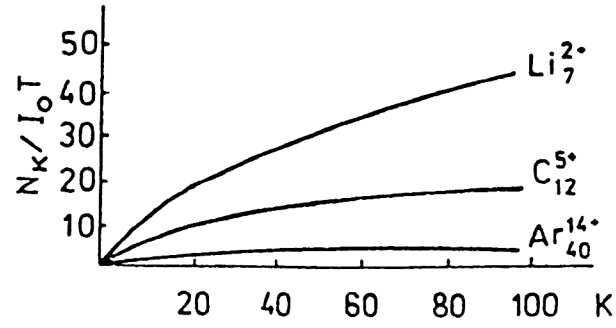

FIG. 23. Ion storage in the Nuclotron booster for charge-exchange injection with a fixed-orbit-bump.[63]

is the probability of formation of ions with equilibrium charge.

Let us consider the case of an exponential law of orbit motion:

$$y_{c0}(t)=y_s e^{-t/\tau}. \tag{4.10.9}$$

Let r be the number of turns during which the orbit moves from the center of the stripper to the center of the machine.

Let us describe the particle storage turn by turn. During the very first turn,

$$N_1=\int_0^T \prod_{j=0}^{r} k(t+jT)I_0 dt \tag{4.10.10}$$

particles are stored in the ring. The multiplication from 0 to r in (4.10.10) describes the successive crossings of the target, while the integration describes the continuous orbital motion. During the second turn the number of stored particles increases to

$$N_2=N_1+\int_T^{2T} \prod_{j=0}^{r-1} k(t+jT)I_0 dt. \tag{4.10.11}$$

In general, we arrive at the following expression for the total number of stored particles:

$$N=\sum_{i=0}^{r}\left\{\int_{iT}^{(i+1)T}\prod_{j=0}^{r-1} k(t+jT)I_0 dT\right\}. \tag{4.10.12}$$

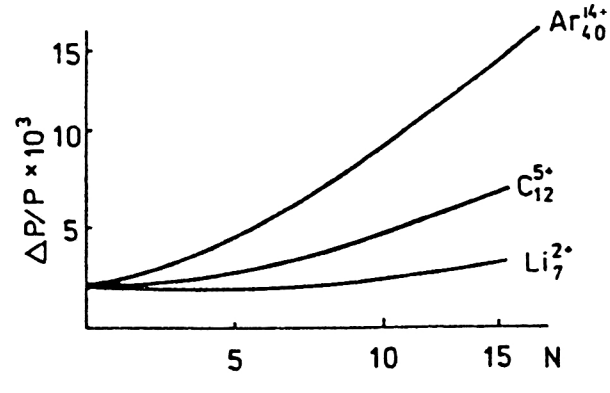

FIG. 22. Additional momentum spread in the Nuclotron booster due to the ionization losses in the stripping target.[63]

4.11. Charge-exchange injection into the Nuclotron booster

As an example, we will give here the simulations of the charge-exchange injection into the Nuclotron booster.[63]

The main booster parameters have been given earlier. Some additional parameters that are important for the injection process are: injection energy for protons, 20 MeV; and for ions with $Z/A=0.5$, it is 5 MeV/n; beam rigidity at injection, 0.647 Tm; injector emittance, 40π mm·mrad; booster acceptance, 260π mm·mrad; momentum spread at injection, $\pm 2\cdot 10^{-3}$.

Some results of the simulation are as follows.

Figure 19 depicts the mean-square angle for multiple scattering in the carbon stripping target.

Figure 20 shows the emittance growth in the Nuclotron booster.

The energy losses for the test ions are plotted in Fig. 21.

The calculated values of the parameter χ are 15 for Ar_{40}^{14+}, 1.9 for C_{12}^{5+}, and 0.3 for Li_6^{2+}. This means that the probability distribution of the ionization losses is normal for heavier ions, while it has Vavilov's form for light ions. Thus, the standard deviation for Ar_{40}^{14+} and for 100-μg/cm^2 thickness of the target is $\sqrt{\gamma x}=39.1$ keV. The calculated standard deviation is 17 keV for C_{12}^{5+} and 5 keV for Li_6^{2+}.

The additional momentum spread due to the ionization losses is given in Fig. 22. The ion storage is shown in Fig. 23.

[1] G. H. Rees, *CERN Accelerator School* (Geneva, 1994), p. 731.
[2] H. Einckhoff *et al.*, *1st EPAC* (Rome, 1988).
[3] D. Reinstad, *2nd EPAC* (Nice, 1990), p. 128.
[4] M. Q. Barton, BNL Preprint BNL-AADD-57 (1964).
[5] S. Fenster *et al.*, IEEE Trans. Nucl. Sci. **NS-28**, 2574 (1976).
[6] J. Claus *et al.*, IEEE Trans. Nucl. Sci. **NS-30**, 342 (1973).
[7] K. Schindl and P. Van der Stok, CERN Preprint MPS/BR Int./74-2 (1974).
[8] P. Van der Stok, CERN Preprint PS/OP/Int. 76-1 (1976).
[9] P. Van der Stok, CERN Preprint PS/OP/77-12 (1977).
[10] C. Bovet and D. Lamotte, CERN Preprint SI/Int. DL/69-13 (1969).
[11] V. Anguelov and D. Dinev, Bulg. J. Phys. No. 4, 56 (1996).
[12] I. B. Issinsky and V. A. Mikhailov, JINR Preprint P1-91-2 (1991).
[13] D. Dinev, Bulg. J. Phys. **20**, No. 3/4, 25 (1993).
[14] V. A. Titov and I. A. Schukeilo, J. Tech. Phys. **38**, 1752 (1968).
[15] A. M. Gromov and P. A. Cherenkov, *13th All-Union Particle Accelerator Conf.* (Moscow, 1973), p. 110.
[16] P. J. Bryant, *CERN Accelerator School* (1989), p. 50.
[17] T. Roser, *4th EPAC* (London, 1994), p. 151.
[18] K. Blasche and B. Franzke, *4th EPAC* (London, 1994), p. 133.
[19] K. Abrahamson *et al.*, *4th EPAC* (London, 1994), p. 380.
[20] K. Symon and A. Sessler, *CERN Symposium on High Energy Accelerators* (1956), Vol. 1, p. 44.

[21] A. Bruckner *et al.*, Nucl. Instrum. Methods **77**, 78 (1970).
[22] E. Ciapala, *CERN Accelerator School* (1984), Vol. 1, p. 195.
[23] B. W. Montague, *1st Int. School on Particle Accelerators* (Etore Majorana Center, 1976).
[24] H. Bruck, *Accélérateurs Circulaires de Particules* (Presses Universitaires, Paris, 1966).
[25] J. Le Duff, *CERN Accelerator School* (1984), Vol. 1.
[26] A. J. Lichtenberg, *Phase-Space Dynamics of Particles* (Wiley, New York).
[27] A. N. Lebedev, Sov. At. Energy **9**, 189 (1960).
[28] K. Symon *et al.*, *Int. Conf. on High Energy Accelerators* (Geneva, 1959), Vol. 1, p. 58.
[29] M. J. de Jonge and E. W. Messerschmidt, IEEE Trans. Nucl. Sci. **NS-20**, 796 (1973).
[30] G. Bisoffi, Ph.D. Thesis, Heidelberg University (1989).
[31] E. Jaeschke *et al.*, *1st EPAC* (Rome, 1988).
[32] G. Bisoffi *et al.*, Nucl. Instrum. Methods **A287**, 320 (1990).
[33] P. A. Chamonard *et al.*, *2nd EPAC* (Nice, 1990).
[34] J. C. Ciret, SATURNE Preprint LNS-SD/MIMAS 88-02 (1988).
[35] G. I. Dimov, Novosibirsk Preprint 304 (1969).
[36] J. D. Simpson, IEEE Trans. Nucl. Sci. **NS-20**, 198 (1973).
[37] K. Hedblom *et al.*, *3rd EPAC* (Berlin, 1992).
[38] S. Martin *et al.*, Nucl. Instrum. Methods **A236**, 249 (1985).
[39] V. S. Nikolaev, *JINR Particle Accelerator School* (1985).
[40] I. S. Dmitriev *et al.*, Nucl. Instrum. Methods **B14**, 515 (1986).
[41] N. Bohr, K. Dan. Vidensk. Selsk. Mat.-Fys. Medd. **18**, No. 8 (1948).
[42] N. Bohr and J. Lindhard, K. Dan. Vidensk. Selsk. Mat.-Fys. Medd. **28**, No. 7 (1954).
[43] S. I. Kozlov, JINR Preprint 9-83-268 (1983).
[44] B. Franzke, *CERN Accelerator School* (1992), p. 100.
[45] J. Alonso *et al.*, IEEE Trans. Nucl. Sci. 1 (1979).
[46] V. P. Zaikov *et al.*, Nucl. Instrum. Methods **B5**, 10 (1984).
[47] E. Baron *et al.*, Nucl. Instrum. Methods **A328**, 177 (1993).
[48] R. B. Clark *et al.*, Nucl. Instrum. Methods **A133**, 17 (1976).
[49] K. J. Xuan and R. Droin, Nucl. Instrum. Methods **160**, 461 (1979).
[50] V. S. Nikolaev and I. S. Dmitriev, Phys. Lett. **284**, 277 (1968).
[51] K. X. To and R. Droin, Nucl. Instrum. Methods **160**, 461 (1979).
[52] K. Shima *et al.*, Nucl. Instrum. Methods **200**, 605 (1982).
[53] H. H. Heckman *et al.*, Phys. Rev. **129**, 1240 (1962).
[54] H. D. Betz *et al.*, Phys. Lett. **22**, 64 (1966).
[55] H. D. Betz, Rev. Mod. Phys. **44**, 465 (1972).
[56] A. I. Abramov, J. A. Kazanskii, and E. C. Matusevich, *Experimental Methods of Nuclear Physics* (Atomizdat, Moscow, 1970).
[57] Y. M. Chirkov and N. P. Yudin, *Nuclear Physics* (Nauka, Moscow, 1974).
[58] K. P. Muchin, *Experimental Nuclear Physics* (Nauka, Moscow, 1974).
[59] T. Joy, Nucl. Instrum. Methods **A106**, 237 (1973).
[60] Particle Data Group, Phys. Lett. **170B**, No. 1 (1986).
[61] L. D. Landau, *Selected Papers* (Moscow, 1969), Vol. 1, p. 482.
[62] P. V. Vavilov, Zh. Éksp. Teor. Fiz. **32**, 920 (1957) [Sov. Phys. JETP **5**, 749 (1957)].
[63] V. Anguelov *et al.*, JINR Preprint E9-94-369 (1994).

This article was published in English in the original Russian journal. It is reproduced here with the stylistic changes by the Translations Editor.